LAWRENCE
LIVERMORE
NATIONAL
LABORATORY

LLNL-JRNL-428242

Non-lethal blast wave interactions with a human head

J.M. Ortega

April 21, 2010

Computers & Fluids

Disclaimer

Non-lethal blast wave interactions with a human head

J. Ortega*

April 19, 2010

Corresponding author: Jason Ortega, Lawrence Livermore National Laboratory, P.O. Box 808, L-184, Livermore, CA 94551; e-mail: ortega17@llnl.gov; phone: 925-423-3824

*Staff Scientist, Engineering, Lawrence Livermore National Laboratory, Livermore, CA.

Abstract

Numerical simulations are used to investigate the transient shock physics and loads that arise when a non-lethal blast wave impinges upon an unprotected human head located atop a complete, anatomically-correct body. Two non-lethal, hemispherical blast waves, each of which corresponds to the detonation of a high explosive charge, are considered for configurations in which the body is facing either towards or away from the explosive charge. The shock wave interactions that arise when the blast wave impinges upon the head are characterized and correlated with the resulting transient surface pressures, forces, and moments on the head. The transient forces and moments are compared to those of an analytical model based upon the work of Zaslavskii, *et al.* [*J. App. Mech. Tech. Phys.*, **42**(3):533-537, 2001], who derived expressions for the drag force on an arbitrary-shaped body due to the interaction with a weak to moderate strength shock wave. The results of this study indicate that Zaslavskii, *et al.'s* model provides a straightforward means of estimating the transient loads on the head during a non-lethal blast wave interaction.

Keywords: blast wave, shock wave interaction, traumatic brain injury

1 Introduction

Traumatic brain injury (TBI) has emerged as the distinguishing injury of the wars in Iraq and Afghanistan [15, 25]. The Defense and Veterans Brain Injury Center estimates that approximately 10 to 20% of all soldiers serving in these wars have suffered some form of TBI [2]. The prevalence of this type of injury is due to the fact that more soldiers are surviving explosive blasts through improvements in body armor and helmets, trauma evacuation, and hospital care [32].

When the human head is exposed to an explosive blast, injuries, such as diffuse axonal injury (DAI), contusions, and subdural hemorrhaging, can occur to the brain [12]. DAI, which is caused by the stretching or tearing of axons, often occurs at the interface of the white and gray matter in the brain and may be produced by high pressure gradients that result when the blast wave passes through this interface [16]. The blast forces can also lead to relative motion between the skull and brain, causing contusions at the locations where the brain impacts the inside of the skull [36]. Additionally, the motion of the brain within the skull can tear veins that bridge the brain surface and the dural venous sinus, leading to traumatic subdural hemorrhaging [35]. Based upon observations that TBI can occur regardless of whether or not the head is protected, others have theorized that TBI is caused when the blast wave passes through the torso into the vascular system, producing pressure oscillations that travel through the arteries and veins into the brain and damage structures close to cerebral vessels [2]. Others hypothesize that the high pressure blast wave ruptures blood vessels, leading to free radical formation that can contribute to an increase in the permeability of the blood brain barrier, cerebral edema, and enhanced inflammatory cellular responses [10]. The end result is that soldiers who are exposed to non-lethal explosive blasts, often without external head injuries, exhibit symptoms of dizziness, difficulty in decision-making, mood swings, fatigue, seizures, memory problems, and sleep deficits [2, 22, 45].

In addition to animal model studies [5, 7, 18], several computational studies have been conducted in order to gain a better understanding of the biomechanics of TBI caused by an explosive blast wave. Mott, *et al.* [29] perform a series of simulations on a helmeted human model, which is comprised of a head and simplified upper torso. The model is positioned three meters away from an explosive charge that produces a non-lethal, yet injurious, blast wave. The results of the simulations reveal that while the helmet protects the forehead, the blast wave can enter the gap between the helmet and the head, leading to high pressures on the back side of the head. Varying the orientation of the model demonstrates that the highest pressures on the head occur when it is positioned at 45° relative to the explosive charge. Moss, *et al.* [28] simulate the exposure of a low fidelity human head and body to a non-lethal blast wave and observe skull deformations that produce pressures and pressure gradients comparable to, if not greater than, those of a TBI arising from an injurious blunt impact. Covering the head with a simplified Kevlar helmet does not reduce the skull deformations since the blast wave enters the gap between the head and the helmet, leading to pressures greater than those of the incident blast wave. Moore, *et al.* [27] and Taylor, *et al.* [38] model the blast effects

on the upper portion of an unprotected human head geometry obtained from magnetic resonance imaging data. In the study of Moore, *et al.*, two blast sizes corresponding to the threshold level and to the 50% lethal dose level for lung injury are considered. The blast waves are observed to propagate into the brain and generate maximum tensile pressures at the sinus, gray matter, cerebral spinal fluid, skull, and white matter. The intracranial pressures produced by the 50% lethal dose blast wave are shown to be comparable to those of a blunt impact that would produce a concussive injury. Taylor, *et al.* expose the head model to a non-lethal blast wave that has a 1.3×10^6 Pa pressure and identify localized regions of elevated pressure and stress within the brain, which may contribute to the development of axonal injury.

While these studies have provided important insights into the potential causes of blast-induced TBI, there remain several unanswered questions regarding the basic shock physics of a non-lethal blast wave interaction with an unprotected human head. For instance, what types of shock wave reflections occur on the outside of the head when the blast wave impinges upon a head situated atop a complete, anatomically-correct body? How do these reflections contribute to the pressure distribution across the surface of the head? What are the resulting forces and moments on the head during the blast wave interaction? And, can an analytical model be developed to provide a straightforward means of estimating the transient blast loads on the head? The purpose of the present study is to address these questions using computational fluid dynamics (CFD) simulations of non-lethal blast wave interaction with a human head positioned on a body.

2 Computational Setup

The model used in this study is a generic, anatomically-correct representation of an adult male, who has a height of 1.829 m and a body volume of 7.42×10^{-2} m^3 (Fig. 1). Assuming a nominal body density of 1046 kg/m^3, the effective mass of the model is $m = 78$ kg [20]. The model is positioned within a hemispherical computational domain in a manner such that the top of the head, which is has a volume, V, of 3.6×10^{-3} m^3, is located at $(r, \theta, \phi) = (4.572$ m , 66.4°, $0^\circ)$. On the ground beneath the model, a slip boundary condition is specified and the velocity, $\mathbf{u}$, pressure, p, and temperature, T, at $z = 0$ are extrapolated from the interior of the computational domain. To reduce the computational resources needed to run the simulations, a symmetry boundary condition is defined on the $\phi = 0^\circ$ and 45° and $\theta = 45^\circ$ planes. Within these planes, the normal gradients of the computed variables are zero and their values are extrapolated from the interior of the computational domain. The symmetry planes at $\phi = 45^\circ$ and $\theta = 45^\circ$ are located sufficiently far from the model such that the shock reflections from the head and body do not reach these planes during the simulation time. By placing a symmetry boundary condition at $\phi = 0^\circ$, we subsequently restrict ourselves to configurations in which the model is facing either directly towards or away from the $x = 0$ plane. At $r = 50$ m, a pressure outlet boundary condition is specified ($p_0 = 101 \times 10^3$ Pa, atmospheric pressure) and $\mathbf{u}$ and T extrapolated from the interior of the computational domain. On the surface of the model, a slip boundary condition is specified.

Two assumptions are made regarding the response of the model to the blast wave, which propagates radially outward from the origin. First, we assume that the deformation of the model is negligible during the blast wave impingement, which is consistent with the results of Moss, *et al.* [28], who showed that the skull deflections are on the order of 50×10^{-6} m during the interaction with a blast wave of comparable overpressure to those of the present study. Second, we assume that the linear and angular displacements of the model centroid are small during the blast wave interaction, thereby allowing us to keep the model at a fixed location in the computational domain. The validity of this approach is evaluated by making the assumption of a fixed, rigid model *a priori*, running the simulations with the largest blast size considered in this study, and measuring the transient blast pressure force, $\mathbf{F}_c$, and moment, M_c, on the model, where M_c is the moment about the $y-$axis at the model centroid, $\mathbf{r}_c$. Using $\mathbf{F}_c = m \cdot d^2\mathbf{r}_c/dt^2$ and $M_c = I_c \cdot d^2\xi/dt^2$, we then estimate what the linear and angular displacements would have been had the model been free to move from rest, where $I_c = 12.9$ kg·m^2 and ξ are the moment of inertia and the angular displacement of the model, respectively, about the $y-$axis at the model centroid. Since the acceleration due to gravity is much less than that due to the blast wave, we do not include gravitational acceleration in the displacement calculations. And for simplicity, the ground force acting on the feet of the model is not considered. The results of this exercise demonstrate that the linear and angular displacements would have been at most 2×10^{-3} m of the model centroid and -0.02 degrees about the model centroid, respectively, over the course of the simulation. Given that the blast wave produces net displacements that are relatively small in comparison to the size of the model, the assumption of employing a fixed model in this study is justified.

2.1 Simulation code

The $\mathbf{u}$, p, T, and density, ρ, fields that arise during the interaction of the blast wave with the model are solved using a finite-volume code, STAR-CCM+ [33]. The air within the computational domain is assumed to be an inviscid, polytropic, ideal gas [8] with a specific heat at constant pressure, c_p, of 1004 J/kg·K and with a value of $\gamma = c_p/c_v = 1.4$, where c_v is the specific heat at constant volume. The time derivatives in the coupled conservation of mass, momentum, and energy equations are discretized with a second-order, explicit, multi-stage, time-stepping scheme [17], while the convective fluxes are evaluated using a second-order, upwind, flux-difference splitting scheme [40, 41]. The time step size is evaluated by means of the Courant number, which has a maximum value of 0.5. The simulations are initialized by setting off a hemispherically-shaped, high explosive (HE) charge that is placed at the origin (Fig. 1). Two HE charge masses, m_{HE} and $5m_{HE}$ (where m_{HE} is equivalent to 0.6 kg of TNT), are considered, both of which are non-lethal for a human in an upright position at this standoff distance [3]. Since the finite-volume code used in this study does not possess the framework for modeling the equation of state of a HE [21], we utilize an alternative approach of replacing the volume filled by the HE with air that has the same specific energy density, E_{HE}, as the HE charge, where E_{HE} would equal 7×10^9 J/m^3 for TNT [9]. The initial pressure, p_{HE}, and temperature,

T_{HE}, of the air within this volume are then obtained from $p_{HE} = E_{HE} \cdot (\gamma - 1)$ and $c_v \cdot T_{HE} = E_{HE}/\rho_0$, respectively, where $\rho_0 = 1.184$ kg/m^3 is the density of air. Additionally, the velocity within this volume is initially zero. Outside of the HE charge, the pressure, temperature, and velocity of air are set to p_0, 300 K, and 0 m/s, respectively. The governing equations are then solved within the computational domain on an unstructured, Eulerian, volumetric polyhedral mesh [33] with a surface resolution of 2×10^{-3} m on the entire surface of the model.

Propagating the blast wave radially outward from the HE charge requires a considerable level of mesh resolution in order to maintain the steep flow field gradients in all three dimensions until the time that the blast wave first impinges upon the model. To avoid the computational expense associated with this approach, we take advantage of the spherical symmetry of the blast wave and utilize a "one-dimensional" spherical mesh, which is one element wide in the $\phi - \theta$ plane and has symmetry boundary conditions on the constant ϕ and θ planes. Using this mesh, the blast wave is propagated in the radial direction from the time $t = 0$ until the time at which the blast wave front is just upstream of the model ($r = 3.95$ m). At that time, the $\mathbf{u}$, p, and T fields from the "one-dimensional" solution are employed as initial conditions for the three-dimensional simulations.

2.2 Code validation

The accuracy of modeling the HE charge as a high temperature and pressure ideal gas is validated by comparing the "one-dimensional" solution with empirical data from a hemispherical surface blast of the same HE charge size (Fig. 2a-b) [39]. A similar validation approach is taken in the blast wave simulations of [6, 29]. The transient pressure profiles used for this comparison are taken from the locations $r = 1.524$, 3.048, and 4.572 m. While there are relatively large differences in the peak pressures and arrival times of the blast wave at the closest radial location, there is better agreement at the larger radial locations, where the initial details of the explosive blast become less important. Repeating the "one-dimensional" simulations on meshes that have an increasing resolution in the radial direction (0.008, 0.004, 0.002, 0.001, and 5×10^{-4} m) demonstrates a mesh-convergent trend, where the shock front Mach numbers, incident pressures, p_i, and relative shock strengths, $\epsilon = (p_i - p_0)/\gamma p_0$, for the two charge sizes are 1.14, 136×10^3 Pa, 0.25, and 1.33, 189×10^3 Pa, and 0.62, respectively, at $r = 4.572$ m. The corresponding shock front Mach numbers, incident pressures, and relative strengths from the empirical data [39] are 1.12, 138×10^3 Pa, and 0.26, and 1.34, 202×10^3 Pa, and 0.71, respectively. The larger difference between the computed and empirical incident pressure for the $5m_{HE}$ charge is understood by calculating the scaled distance, $Z = r/m_{HE}{}^{\frac{1}{3}}$ and $r/(5m_{HE})^{\frac{1}{3}}$, at $r = 4.572$ m for the two charge sizes, respectively [6, 14, 19]. Since Z is smaller for the $5m_{HE}$ charge, the physics of the HE detonation process that are not entirely captured by the ideal gas equation of state have a slightly greater influence on the blast wave properties at $r = 4.572$ m than those of the m_{HE} charge, which is at a larger scaled distance.

To determine the accuracy of the finite-volume code in predicting the transient forces that arise during the blast wave interaction with the model, we perform a validation simulation on the interaction of a planar shock wave with a sphere. In the study of Tanno, *et al.* [37], a 0.08 m diameter sphere is placed within a shock tube and exposed to a planar shock of Mach number 1.22, which is comparable to the blast wave Mach numbers at $r = 4.572$ m in the present study. We simulate this experimental setup within an axi-symmetric computational domain using the modeling approach described previously and make a comparison between the computed and experimental drag force coefficient on the sphere. The time $t = 0$ is taken to be the instant at which the shock wave arrives at the frontal stagnation point, $\alpha = 0^\circ$. There is fair agreement between the computed and experimental drag force coefficient, $C_{x'}$, during the shock wave interaction, where $C_{x'} = F_{x'}/\frac{1}{2}\rho_i U_i^2 S_0$, $F_{x'}$ is the drag force on the sphere, $\rho_i = 1.66$ kg/m^3 and $U_i = 114$ m/s are the fluid density and velocity, respectively, behind the incident shock front, and $S_0 = \frac{\pi}{4}(0.08)^2$ is the maximum cross-sectional area of the sphere (Fig. 3a). The present simulations even capture the negative drag force coefficient that arises during the latter portion of the shock wave interaction.

2.3 Drag and lift force model

The drag force coefficient of the sphere is also compared to the theoretical model of Zaslavskii, *et al.* [44], which estimates the force on an arbitrary-shaped body during the interaction with a weak to moderate strength ($\epsilon < 0.3 - 0.5$) planar shock wave. Using the theory of geometrical acoustics [11], Zaslavskii, *et al.* provide an estimate for the transient decay of the reflected shock wave pressure on the surface of a body, which is divided into two regions. The first region, σ_r, is defined to be that which corresponds to the angles of shock wave incidence $\frac{2}{3}\beta^* < \beta < \frac{\pi}{2}$ where regular reflection ($\beta^* < \beta < \frac{\pi}{2}$) and Mach reflection ($\frac{2}{3}\beta^* < \beta < \beta^*$) occur, where $\beta = \frac{\pi}{2} - \alpha$, α is as shown in Fig. 3a, and β^* is the minimum angle of incidence (critical angle) for which regular reflection is possible [8]. The second region, σ_t, corresponds to the angles of incidence $-\frac{\pi}{2} < \beta < \frac{2}{3}\beta^*$ where Mach reflection ($0 < \beta < \frac{2}{3}\beta^*$) and shock wave diffraction ($-\frac{\pi}{2} < \beta < 0$) occur. The portion of σ_r intersected by the shock is taken to have a surface pressure equal to

$$p_{\sigma_r} = p_i + \frac{p_{nr} - p_i}{\left(1 + N_i(t - t_0)/\delta_0\right)^\omega} \tag{1}$$

while the portion of σ_t intersected by the shock is taken to have a surface pressure of $p_{\sigma_t} = p_i$, where N_i is the speed of the incident shock wave, δ_0 is the characteristic radius of curvature of the body, t_0 the time when the shock wave first makes contact with the body at $\beta = \frac{\pi}{2}$, ω is a damping coefficient that is equal to 0.5 for a cylinder and 1.0 for a sphere,

$$p_{nr} = p_0 + (p_i - p_0)\left[1 + \frac{1 + \mu^2}{\frac{p_0}{p_i} + \mu^2}\right] \tag{2}$$

is the pressure due to normal reflection of the shock wave, and $\mu^2 = (\gamma - 1)/(\gamma + 1)$ [8]. Zaslavskii, *et al.*

show that the resulting transient force, $F_{x'}$, on the body in the direction of the shock wave propagation, x', can be approximated by

$$F_{x'} = \left[(p_i - p_0) + \frac{p_{nr} - p_i}{\left(1 + N_i(t - t_0)/\delta_0\right)^{\omega}}\right] S_{x'}(t) \tag{3}$$

for $t\Big|_{\beta=\frac{\pi}{2}} < t < t\Big|_{\beta=\frac{2}{3}\beta^*}$ and by

$$F_{x'} = (p_i - p_0) S_{x'}(t) + \frac{p_{nr} - p_i}{\left(1 + N_i(t - t_0)/\delta_0\right)^{\omega}}\ S_{x'rt} \tag{4}$$

for $t\Big|_{\beta=\frac{2}{3}\beta^*} < t < t\Big|_{\beta=-\frac{\pi}{2}}$, where $S_{x'}(t)$ is the transient cross-sectional area of the body in the x' plane intersected by the shock wave front on either region σ_r or σ_t and $S_{x'rt}$ is the cross-sectional area in the x' plane intersected by the shock wave front at $t\Big|_{\beta=\frac{2}{3}\beta^*}$. In Eq. 3, the first term is due to the overpressure of the incident shock wave, while the second term arises from the reflection of the incident wave and decays in time according to the theory of geometrical acoustics. After the incident wave passes beyond $\beta < \frac{2}{3}\beta^*$, the pressure force on σ_t is due only to the incident overpressure, which is the first term in Eq. 4. The second term in Eq. 4 is the additional force on σ_r due to the reflected pressure, which continues to decay as $t^{-\omega}$. Zaslavskii *et al.'s* theory can also be extended to provide an estimate of the lift force, $F_{y'}$, perpendicular to the direction of shock wave propagation. For this estimate, the area, $S_{x'}(t)$, in Eqs. 3-4 is replaced with the projected cross-sectional area, $S_{y'}(t)$, in a y' plane intersected by the shock. Similarly, $S_{x'rt}$ is replaced with the projected cross-sectional area, $S_{y'rt}$, in a y' plane of the entire σ_r region. For a completely enclosed body, such as a sphere, the net lift force is predicted to be zero by Eqs. 3-4 since equal pressures are assumed to act on both sides of $S_{y'}(t)$ and $S_{y'rt}$ during the entire shock wave interaction. Thus, the only means Zaslavskii *et al.'s* model can produce a finite force in the y'-direction is by evaluating Eqs. 3-4 on an unenclosed body. In that case, the sign of $S_{y'}(t)$ and $S_{y'rt}$ is understood to be *positive* for the unenclosed cross-sectional area with a normal vector in the $+y'$-direction and *negative* for the unenclosed cross-sectional area with a normal vector in the $-y'$-direction.

In the experiment conducted by Tanno, *et al.* [37], $p_0 = 101 \times 10^3$ Pa and $p_i = 159 \times 10^3$ Pa, giving a value of $\epsilon = 0.41$, which is within the range of applicability of Eqs. 3-4. In addition, the speed of the incident shock wave is $N_i = 414$ m/s, the critical angle of incidence is $\beta^* \approx 33^\circ$ [1, 37], and the radius of curvature of the sphere is $\delta_0 = 0.04$ m. Inserting these values and those of $S_{x'}(t)$ and $S_{x'rt}$, which are obtained from the present validation simulation of Tanno, *et al.*, into Eqs. 3-4 produces a transient drag force coefficient curve (Fig. 3a), which captures the general trend of the experimental data, but over-predicts the magnitude of $C_{x'}$. We use Eqs. 3-4 to estimate the lift force on only one half ($y' \geq 0$) of the sphere, such that $S_{y'}(t)$ and $S_{y'rt}$ are taken to be negative on the downward facing, unenclosed cross-sectional area. A comparison of the lift force coefficient, $C_{y'} = F_{y'}/\frac{1}{2}\rho_i U_i^2 S_0$, in the y'-direction with the corresponding simulation results indicates that Eqs. 3-4 capture the initial trend of $C_{y'}$ (Fig. 3b). However, the magnitude of $C_{y'}$ is over-predicted

at later times. A plot of $p(\alpha)$ (Fig. 3b, inset) demonstrates that these discrepancies in $C_{x'}$ and $C_{y'}$ are produced by theoretical pressure values on both σ_r and σ_t that can be greater than those of the simulation results.

Despite these differences, we anticipate that Zaslavskii, *et al.'s* model may offer a rather simple means of approximating the transient force on the head during the blast wave interaction. Equations 3-4 can also be modified to estimate the moment produced by the blast wave on the head. In Section 3.3, we derive the theoretical moment using Eqs. 3-4 and make a comparison between the predicted forces and moment and those of the present computational study.

2.4 Mesh refinement simulations

Having determined the accuracy of the finite-volume code in both propagating a hemispherical blast wave and predicting the force during a shock wave interaction, we conclude this section by performing a mesh refinement study for the three-dimensional computational domain ($0 \leq r \leq 50$ m, $0^\circ \leq \phi \leq 45^\circ$, $45^\circ \leq \theta \leq 90^\circ$). While a 0.001 m radial resolution is sufficient for propagating the blast wave from the HE charge to the model on a "one-dimensional" mesh, this high level of spatial resolution is not necessarily required at the nominal radial location of the model head ($r = 4.572$ m). To determine what resolution is needed, we perform simulations in the three-dimensional domain with mesh resolutions of 0.016, 0.008, and 0.004 m in the volume surrounding the upper portion of the model. The simulation is initialized with the $\mathbf{u}$, p, and T fields from the 0.001 m resolution, "one-dimensional" solution at a time when the blast wave front is just upstream of the feet of the model ($r = 3.95$ m). This exercise is repeated on four configurations: m_{HE} charge, no model present; $5m_{HE}$ charge, no model present; m_{HE} charge, frontal-facing model present; and $5m_{HE}$ charge, frontal-facing model present. The blast pressure profiles for the first two configurations exhibit a mesh-convergent trend and compare favorably with the pressure profiles from the corresponding "one-dimensional" solution (Fig. 2a-b, inset). Additionally, the pressures across the surface of the model head for the last two configurations exhibit a mesh-convergent trend for both blast sizes (Fig. 4). Therefore, the 0.008 m resolution meshes are used in this study.

3 Results and Discussion

The simulations for the 35×10^3 and 88×10^3 Pa overpressure ($p_i - p_0$) blast waves are run until $t = 11.3\times10^{-2}$ and 9.9×10^{-3} s, respectively, at which time the blast waves have propagated downstream of the model. In the following sections, the resulting shock wave reflections that arise when the blast wave impinges upon the head are characterized and correlated with the transient surface pressures, forces, and moments on the head.

3.1 Blast wave interactions

When the blast wave strikes the model, it produces a number of shock wave reflections from the head. For the frontal blast cases, the first reflection from the head, which arises at the locus R_1, begins when a portion of the incident wave, w_i, impinges directly upon the chin and mouth (Figs. 5a, 6a) to form a reflected shock wave, w_{cm}, which has a varying curvature due to the complexity of the facial features. A portion of the incident wave advances beneath the chin and reflects from the neck at the locus R_n (Fig. 6b). The resulting reflected wave, w_n, propagates in the -$x-$direction and expands down the chest and up to the chin. As the remaining portion of the incident wave passes over the concave indentations formed by the eye sockets, the wave is both focused and reflected. Within the $y = 0$ plane, this reflection generates two waves that originate from the top, w_{es_t}, and bottom, w_{es_b}, of the eye sockets (Fig. 6b). At later times, these two waves merge to form a single reflected shock front, w_{es} (Fig. 6c). A Mach stem, M_h, forms on w_i and w_{es} at the top of the forehead (Fig. 6c) at $d_{nh} \approx 0.4$ m ($\alpha \approx 85°$), where d_{nh} and α are shown in Fig. 6f and α is defined to be the angle relative to the line joining the center of gravity (c.g.) of the head to the origin of the computational domain. The locus of the resulting triple point, T_p, which is identified by fitting the w_i and w_{es} waves in the $y = 0$ plane with two second-order polynomials and by computing their intersection point, is a straight line oriented at approximately 36° with respect to the line, x', joining the origin to the centroid of the head (or about 60° to the horizontal, Fig. 6c-d). This triple point path angle is comparable to that resulting from the interaction of a shock wave with a circular cylinder or sphere. For these simpler geometries, the triple point nominally follows a straight line that is oriented at approximately 30° to 34° with respect to the axis of symmetry [4, 13, 31, 42, 43, 46]. Due to local variations in surface curvature and multiple reflections that occur along the neck, a single Mach stem does not develop uniformly over the entire head and neck. Consequently, the Mach stem, M_n, emerging at the back of the neck does not necessarily originate at the same time as M_h. Eventually, these Mach stems completely envelop the entire head, though due to varying amounts of shock diffraction, this envelopment does not take place at a single point, as evidenced by the μ-shaped signature, μ_e, in the density gradient field at the back of the head (Figs. 5f, 6e).

The second most predominant reflection from the head arises as a result of the incident wave that reflects off the front of the torso at the locus R_2, forming the wave, w_t (Figs. 5b, 6a). Moss, *et al.* [28] and Mott, *et al.* [29] observe a similar type of reflection from a simplified model of a human head and torso. The w_t wave travels up the chest and neck, where it impinges normally upon the lower jaw, producing a reflected wave, w_j, at the locus R_j (Fig. 6c). Continuing its upward motion over the face and head, w_t produces additional reflections from eye-sockets (Fig. 6e). At much later times (not shown), w_t detaches from the top of the head and merges with a Mach stem that is produced following the envelopment of the head by the Mach stems, M_h and M_n.

A similar sequence of events is present for the blast wave striking the back of the head (Fig. 5g-j, 7a-d).

Initially, a regular reflection of the incident wave forms the reflected wave, w_{bh}. Though due to a smoother surface topology, fewer reflections occur as the incident wave passes over the back of the head. A Mach stem, M_h, develops on the w_i and w_{bh} waves within the $y = 0$ plane at $d_{nh} \approx 0.5$ m (Fig. 7b). Similar to the frontal blast configuration, the locus of the resulting triple point is also approximated by a straight line oriented at approximately 36° with respect to the line joining the origin to the centroid of the head (or about 60° to the horizontal, Fig. 7d).

3.2 Blast wave pressure signatures

These blast wave interactions lead to distinct transient pressure signatures across the surface of the head. The incident wave from the frontal blast initially generates a concentrated pressure increase that is centered on the mouth (Fig. 6f, $d_{nh} \approx 0.2$ m). This pressure signature quickly spreads within the $y = 0$ plane as the incident wave continues its motion over the head and below the chin. At sites of multiple reflections, constructive interference produces significantly elevated surface pressures. This is especially evident when the w_t wave interferes with the waves that have been reflected from the neck and the base of the jaw (Fig. 6g, $d_{nh} = 0.075$ m; Fig. 6h, $d_{nh} = 0.14$ m). The resulting instantaneous surface pressures on the throat and chin are greater than the reflected pressure, p_{nr} (Eq. 2), that would have been generated had the incident wave normally reflected off of the surface at $r = 4.572$ m. The pressure also increases as the incident wave travels over the eye-sockets (Fig. 6g, $d_{nh} = 0.29$ m). For points downstream of the location where the Mach stems first form (Fig. 4c-f, i-l), the pressure approximately follows the behavior of the incident pressure of an isolated blast wave. However, when the Mach stems converge, a local maximum in pressure occurs at the μ_e location (Fig. 6j, $d_{nh} = 0.58$ m), an observation also seen for the interaction of a blast wave with a bomb suit helmet [24] and during the convergence of Mach stems at the rear stagnation point of a circular cylinder [13] or a sphere [37]. For the backward facing blast, the pressure at the junction of the neck and base of the head also exceeds p_{nr} when constructive interference arises between the w_t wave and the wave, w_{bh}, that is reflected from the back of the head (Fig. 7e, $d_{nh} = 0.7$ m). Shock diffraction due to presence of the neck and body is especially evident for the backward facing orientation at the front of the neck (Fig. 8f), where there is a distinct lag between the arrival time of the Mach stem and the isolated incident blast wave. In a manner similar to that of the frontal blast, points located downstream from where the Mach stem forms (Fig. 8c-e) are subjected to pressures that are comparable to those of an isolated blast wave. Additionally, a local maximum in pressure arises on the forehead at the μ_e location when the Mach stems converge (Fig. 7h, $d_{nh} \approx 0.35$ m).

Further details of these blast wave interactions are obtained by means of spatial-temporal plots of the pressure along the head and neck at $y = 0$. The plots for the two frontal blast cases (Fig. 9a,c) appear qualitatively similar and reveal that pressures in excess of $p_0 + 0.5(p_{nr} - p_0)$ arise from the neck to nearly the top of the head ($d_{nh} < 0.4$ m) within approximately the first 0.7×10^{-3} s after the initial impingement of

the incident wave upon the mouth of the model. After the passage of the incident wave, there is a decrease in pressure below $p_0 + 0.5(p_{nr} - p_0)$ from the base of the jaw to the nose ($d_{nh} = 0.15$ to 0.25 m) followed by a secondary increase due to the arrival of the w_t wave. When the Mach stems converge at the μ_e location ($d_{nh} \approx 0.57$ m, $t = 8.1 \times 10^{-3}$ s for the 35×10^3 Pa overpressure blast wave; $d_{nh} \approx 0.57$ m, $t = 5.9 \times 10^{-3}$ s for the 88×10^3 Pa overpressure blast wave), the pressure momentarily increases above $p_0 + 0.5(p_{nr} - p_0)$ for both frontal blast cases. The pressure eventually drops below atmospheric pressure, as would be expected due to the negative phase of the blast wave. For the 88×10^3 Pa overpressure blast wave, there is a small region at the back of the neck ($d_{nh} = 0.62$ to 0.72 m, $t = 6.6 \times 10^{-3}$ to 8.7×10^{-3} s) that experiences pressures as low as 70×10^3 Pa due to flow separation arising from the induced motion of a counter-rotating vortex pair (not shown) that originates from the base of the head. The appearance of this vortex pair may, perhaps, be a three-dimensional counterpart of the vortical structures observed in Ofengeim & Drikakis [31] for the interaction of a blast wave with a circular cylinder.

For the two backward facing cases, the spatial-temporal plots also appear qualitatively similar to one another (Fig. 9b,d). Pressures in excess of $p_0 + 0.5(p_{nr} - p_0)$ exist across the back of the neck and head ($d_{nh} > 0.5$ m) over the first 0.4×10^{-3} s following the impingement of the incident wave upon the back of the head. However, unlike the frontal facing case of the 88×10^3 Pa overpressure blast wave, there is no sub-atmospheric pressure signature at $y = 0$ from the counter-rotating vortex pair. In this case, the vortex pair forms on either side of the neck (not shown), producing sub-atmospheric pressures at the junction of the jaw and the head. Additionally, the pressure remains below $p_0 + 0.5(p_{nr} - p_0)$ when the Mach stems converge at the μ_e location.

3.3 Transient forces and moments

These shock wave interactions produce transient forces (Fig. 10) on the head that are computed from $\mathbf{F} = -\int_{S_h} p\mathbf{n}\, dS$ where $\mathbf{n}$ is the unit normal of the head surface and S_h is the surface area of the head. For the frontal blast cases, the force, $F_{x'}$, on the head in the x'-direction rises to a maximum value when the w_i wave approaches the top of the forehead ($d_{nh} \approx 0.4$ m). In the backward facing blast cases, a similar trend occurs in which F'_x has a maximum value when the w_i wave is located near the top of the head ($d_{nh} \approx 0.5$ m). As the w_i wave travels to the downstream side of the head, $F_{x'}$ decreases and, at later times, reverses sign and falls to a minimum value that is less than zero, a result which is similar to the negative drag values that arise during the latter stage of a shock wave interaction with a sphere or cylinder [23, 31, 34, 37]. The force, $F_{z'}$, in the z'-direction is negative while the blast wave propagates over the head. In both frontal facing cases, a local maximum in $F_{z'}$ occurs when the vertically traveling w_t wave reflects off of the jaw at $t = 7.64 \times 10^{-3}$ and 5.50×10^{-3} s for the 35×10^3 and 88×10^3 Pa overpressure blast waves, respectively. Due to a smoother geometric transition from the neck to the head, this local maximum is not present for the backward facing cases. The maximum value of the total force on the head, $F_{x'z'} = \sqrt{F_{x'}^2 + F_{z'}^2}$, increases by

about three times as the blast overpressure is increased from 35×10^3 to 88×10^3 Pa for each body orientation. However, by using the Buckingham-Pi theorem [30], it can be shown that the non-dimensional maxima of $F_{x'z'}$ are relatively independent of the HE charge size and are equal to $C(\rho_0\ c_0^2\ E_0^2)^{\frac{1}{3}} = C(\gamma p_0 \cdot E_0^2)^{\frac{1}{3}}$, where c_0 is the speed of sound in the quiescent fluid, $E_0 = E_{HE} \cdot m_{HE}/\rho_{HE}$ (or $E_{HE} \cdot 5m_{HE}/\rho_{HE}$) is the energy of the HE charge, ρ_{HE} is the density of the HE charge (which would equal to 1600 kg/m^3 for TNT [9]), and C is a constant of proportionality that is found from Fig. 10 to equal 0.001 for both blast sizes and body orientations.

The forces that arise on the head during the blast wave interaction can be compared with those predicted by the analytical model of Zaslavskii, *et al.* [44]. However before applying this model to the present study, a number of assumptions must be made. The first is that the incident blast waves are weak to moderate in strength, *i.e.*, $\epsilon < 0.3 - 0.5$. While this is true at the nominal location of the head ($r = 4.572$ m) for the 35×10^3 Pa overpressure blast wave in which $\epsilon = 0.25$, it is not true for the 88×10^3 Pa overpressure blast wave in which $\epsilon = 0.62$. Therefore, discrepancies may arise between the theoretical and computational force values. Second, the assumption is made that the shock front speed, N_i, does not decrease significantly while the blast wave passes over the head, thereby allowing this quantity to be taken as a constant in Eqs. 3-4. Evaluation of the isolated blast simulations reveals that at $r = 4.572$ m, N_i is equal to 397 and 460 m/s for the 35×10^3 and 88×10^3 Pa overpressure blast waves, respectively, and that these values are constant to within less than 0.5% over the period of time during which the incident blast wave intersects the head. On the other hand, the incident pressure, p_i, decreases by as much as 15% from its initial value over the same time period for the 88×10^3 Pa overpressure blast wave. Thus, Eqs. 3-4, which assume a constant value for p_i, may produce values of $F_{x'}$ and $F_{z'}$ that are larger in magnitude than those of the simulations. The next assumption is that the transition from regular to Mach reflection of the incident blast wave occurs at one instant in time over the entire head. Due to the geometric complexity of the head surface and the multiple shock reflections, transition does not occur simultaneously across the entire head, as would be the case for an isolated, axi-symmetric body, such as a sphere. Therefore, the definition of a single critical transition angle, $\beta^* = \frac{\pi}{2} - \alpha^*$, is somewhat subjective. For the sake of this exercise, β^* is taken to be the angle at which the Mach stem, M_h, first forms on the w_i and w_{es} waves at $y = 0$. The resulting values of β^* are approximately 12° and 23° for the frontal and backward facing cases, respectively, with the 35×10^3 Pa overpressure blast wave and approximately 16° and 24° for the frontal and backward facing cases, respectively, with the 88×10^3 Pa overpressure blast wave. The final assumption is that the incident blast wave can be approximated by a planar shock front at $r = 4.572$ m. If the nominal radius of curvature of the head, δ_0, is calculated from $V = \frac{4}{3}\pi\delta_0^3$, where V is the volume of the head, the quantity, $\delta_0/4.572$ m, is found to be equal to 0.02, indicating that the curvature of the blast wave front can be safely ignored for the head at this standoff distance.

With these assumptions in mind, we calculate the transient force on the head predicted by Eqs. 3-4,

where ω is set to 1 and p_i is taken to be the incident pressure at the location when the w_i wave first intersects the head ($d_{nh} = 0.167$ m and 0.662 m for the frontal and backward facing cases, respectively). The values of $S_{x'}(t)$, $S_{x'rt}$, $S_{z'}(t)$, and $S_{z'rt}$ are obtained from the simulations and computed in such a manner as to account for the geometric shielding effect that the neck has upon the lower, downstream portion of the head. As is evident in Fig. 10, Zaslavskii, *et al.'s* model captures the behavior of the transient forces on the head fairly well, though it distinctly over-predicts the maximum values of $|F_{x'}|$ and $|F_{z'}|$ for both frontal facing cases.

The moment imparted to the head by the blast wave is also calculated from the simulations using the relationship $M_{oc}\mathbf{e}_y = -\int_{S_h}(\mathbf{r} - \mathbf{r}_{oc}) \times p\mathbf{n}\ dS$, where $\mathbf{e}_y$ is the unit vector in the y-direction and $\mathbf{r}_{oc}$ is taken to be the rotational point of the head at the base of the skull, which is approximately the location of the occipital condyles (Fig. 11a) [26]. For the frontal blast cases, M_{oc} (Fig. 11a-b) is initially positive and increases to a local maximum when the incident wave is located at the top of the forehead ($d_{nh} = 0.4$ m). This is followed by a secondary increase to an overall maximum value, which occurs as the vertically travelling w_t wave reflects off of the jaw and provides an additional contribution to M_{oc}. As the Mach stems travel to the back of the head, M_{oc} decreases and eventually becomes negative. Aside from lacking two local maxima, the trends in M_{oc} for the backward facing cases appear qualitatively similar to those of the frontal blast cases (Fig. 11c-d). Like $F_{x'}$ and $F_{z'}$, M_{oc} is based upon the surface integral of the blast pressure across the head and, thus, when normalized by $|\mathbf{r}_{cg} - \mathbf{r}_{oc}|(\gamma p_0 \cdot E_0^2)^{\frac{1}{3}}$, the maxima of M_{oc} collapse to values about equal to 0.001 for both blast sizes and body orientations, where $|\mathbf{r}_{cg} - \mathbf{r}_{oc}| = 5.71 \times 10^{-2}$ m is the distance from the center of gravity of the head to the occipital condyles.

Lastly, a comparison can be made between the simulated moment and that from Zaslavskii, *et al.'s* model through a modification of Eqs. 3-4. We take the center of pressure of the blast force on the head to be located at $\mathbf{r}_{cp}(t) = (x'_{cp}(t), 0, z'_{cp}(t))$, where $x'_{cp}(t)$ is the x' component of the area centroid of $S_{z'}(t)$ and $z'_{cp}(t)$ is the z' component of the area centroid of $S_{x'}(t)$. It then follows that the moment on the head about the occipital condyles can be estimated from

$$M_{oc}\mathbf{e}_y = \Big(\mathbf{r}_{cp}(t) - \mathbf{r}_{oc}\Big) \times \left[(p_i - p_0) + \frac{p_{nr} - p_i}{\big(1 + N_i(t - t_0)/\delta_0\big)^{\omega}}\right]\Big(S_{x'}(t)\ \mathbf{e}_{x'} + S_{z'}(t)\ \mathbf{e}_{z'}\Big) \tag{5}$$

for $t\Big|_{\beta=\frac{\pi}{2}} < t < t\Big|_{\beta=\frac{2}{3}\beta^*}$ and by

$$M_{oc}\mathbf{e}_y = \Big(\mathbf{r}_{cp}(t) - \mathbf{r}_{oc}\Big) \times (p_i - p_0)\Big[S_{x'}(t)\ \mathbf{e}_{x'} + S_{z'}(t)\ \mathbf{e}_{z'}\Big]\ +$$

$$\Big(\mathbf{r}_{cp}(t\Big|_{\beta=\frac{2}{3}\beta^*}) - \mathbf{r}_{oc}\Big) \times \frac{p_{nr} - p_i}{\big(1 + N_i(t - t_0)/\delta_0\big)^{\omega}}\Big[S_{x'rt}\mathbf{e}_{x'} + S_{z'rt}\mathbf{e}_{z'}\Big] \tag{6}$$

for $t\Big|_{\beta=\frac{2}{3}\beta^*} < t < t\Big|_{\beta=-\frac{\pi}{2}}$. It is evident from Fig. 11 that this theoretical moment nominally follows the trends of the simulated moment, but over-predicts the maxima for both the frontal and backward facing

cases. In addition, the secondary increase in M_{oc} due to the reflection of the w_t wave off of the jaw for the frontal facing cases is not present since Eqs. 5-6 account only for the moment due to the incident blast wave.

4 Conclusions

Through this computational study, we have investigated the interactions of non-lethal, hemispherical blast waves with the front and back of a human head situated atop an anatomically-correct body. For the blast sizes and body orientations considered, the predominant shock wave interactions with the head arise from the reflection of both the incident blast wave and the shock wave that is reflected from the torso. Constructive interference from multiple shock reflections at the junction of the head and neck for either body orientation produces local surface pressures that are significantly greater than that of a normal reflection of the incident blast wave. On the other hand, the surface pressure on the downstream side of the head is approximately equal to the transient incident pressure of an isolated blast wave during the majority of the interaction. Though, an increase in pressure is observed to occur at a localized region on the downstream side of the head where the Mach stems converge upon themselves. For the orientation in which the body faces the blast, the added geometric complexity of the facial features produces further shock wave reflections and interactions, resulting in elevated surface pressures across such areas as the eye-sockets and brow.

The transient forces and the moment on the head about the base of the skull are evaluated from the simulation data. Within 0.2×10^{-3} to 0.4×10^{-3} s following the impingement of the blast wave, the net force and the moment on the head reach maximum values, which when properly non-dimensionalized, collapse to single values for both body orientations and blast sizes. As the incident blast wave continues to envelop the head, the drag force and moment quickly decrease and reverse sign. We apply Zaslavskii, *et al.'s* force calculation model to the head geometry and modify the model to compute the moment on the head during the blast wave interaction. A comparison between the analytical and simulated results demonstrates that Zaslavskii, *et al.'s* model captures the general behavior of the forces and moments on the head for both the frontal and backward facing non-lethal blast wave interactions.

5 Acknowledgments

The author would like to thank W. Moss and M. King of Lawrence Livermore National Laboratory (LLNL) for the opportunity to collaborate on the traumatic brain injury research effort at LLNL, J. Hartman for his clinical input on cranio-vertebral biomechanics, D. Maitland for his discussion on shock wave-solid body interactions, J. Rodriguez for her assistance in the background literature survey and in the preparation of the human model geometry, K. Salari for his guidance on the simulations, and W. Small for his helpful feedback in the manuscript preparation. This work was performed under the auspices of the US DOE by LLNL under

contract DE-AC52-07NA27344.

References

[1] Ben-Dor, G., *Shock wave reflection phenomena*, 2nd Edition, Springer-Verlag, New York, 2007.

[2] Bhattacharjee, Y., Shell shock revisited: solving the puzzle of blast trauma, *Science*, **319**:406-408, 2008.

[3] Bowen, I.G., Fletcher, E.R., Richmond, D.R., Estimate of man's tolerance to the direct effects of air blast, Defense Atomic Support Agency, Report DASA-2113, 1968.

[4] Bryson, A.E., Gross, R.W., Diffraction of strong shocks by cones, cylinders, and spheres, *JFM*, **10**(1):1-16, 1961.

[5] Cernak, I., *et al.*, Ultrastructural and functional characteristics of blast injury-induced neurotrauma, *Journal of Trauma Injury, Infection, and Critical Care*, **50**(4):695-706, 2001.

[6] Chapman, T.C., Rose, T.A., Smith, P.D., Blast wave simulation using AUTODYN2D: a parametric study, *Int. J. Impact Engng.*, **16**(5/6):777-787, 1995.

[7] Chavko, M., Measurement of blast wave by a miniature fiber optic pressure transducer in the rat brain, *Journal of Neuroscience Methods*, **159**:277-281, 2007.

[8] Courant, R., Friedrichs, K.O., *Supersonic flow and shock waves*, Interscience Publishers, Inc., New York, 1948.

[9] Dobratz, D.M., Crawford, P.C., LLNL explosives handbook: properties of chemical explosives and explosive stimulants, UCRL-52997, 1985.

[10] Elsayed, N.M., Gorbunov, N.V., Kagan, V.E., A proposed biochemical mechanism involving hemoglobin for blast overpressure-induced injury, *Toxicology*, **121**:81-90, 1997.

[11] Friedlander, F., *Sound Pulses*, Cambridge, 1958.

[12] Gutierrez-Cadavid, J.E., Imaging of head trauma, in *Imaging of the Nervous System*, Eds. Latchaw, R.E., Kucharczyk, J., Moseley, M.E., Elsevier Mosby, 869-904, 2005.

[13] Heilig, W.H., Diffraction of a shock wave by a cylinder, *Phys. Fluids*, **S1**(2):154-157, 1969.

[14] Held, M., Blast waves in free air, *Propellants, Explosives, Pyrotechnics*, **8**:1-7, 1983.

[15] Hoge, C.W., *et al.*, Mild traumatic brain injury in U.S. soldiers returning from Iraq, *NEJM*, **358**(5):453-463, 2008.

[16] Imielinska, C., Przekwas, A., Tan, X.G., Multi-scale visual analysis of trauma injury, *Information Visualization*, **5**:279-289, 2006.

[17] Jameson, A., Schmidt, W., Turkel, E., Numerical solution of the Euler equations by finite volume methods using Runge-Kutta time stepping schemes, AIAA Paper 81-1259, 1981.

[18] Kato, K., Pressure-dependent effect of shock waves on rat brain: induction of neuronal apoptosis mediated by a caspase-dependent pathway, *J Neurosurg*, **106**:667-676, 2007.

[19] Kinney, G.F., Graham, K.J., *Explosive shocks in air*, 2nd Edition, Springer-Verlag, New York, 1985.

[20] Krzywicki, H.J., Chinn, K.S.K., Human body density and fat of an adult male population as measured by water displacement, US Army Medical Research and Nutrition Laboratory, Report No. 297, 1966.

[21] Lee, E.L., Hornig, H.C., Kury, J.W., Adiabatic expansion of high explosive detonation products, UCRL-50422, Lawrence Radiation Laboratory, 1968.

[22] Lemonick, M.D., War head injuries: long-term effects, *Time*, http://www.time.com/time/health/article/0,8599,1708624,00.html, 2008.

[23] Lyakhov, V.N., Interaction of moderately strong shock waves with a cylinder, translated from *Izvestiya Akademii Nauk SSSR, Mekhanika Zhidkosti i Gaza*, **2**:113-119, 1979.

[24] Mathis, J.T., Clutter, J.K., Evaluation of orientation and environmental factors on the blast hazards to bomb suit wearers, *Applied Ergonomics*, **38**:567-579, 2007.

[25] McCracken, D.L., Traumatic brain injury emerging as the distinguishing injury of the Iraq war, *US Veteran Brain Injury News*, http://www.birf.info/home/library/vet/vet-tbi-iraq.html, 2005.

[26] Menezes, A.H., Traynelis, V.C., Anatomy and biomechanics of normal craniovertebral junction (a) and biomechanics of stabilization (b), *Childs Nerv Syst*, **24**:1091-1100, 2008.

[27] Moore, D.F., *et al.*, Computational biology - modeling of primary blast effects on the central nervous system, *NeuroImage*, **47**(S2):T10-T20, 2009.

[28] Moss, W.C., King, M.J., Blackman, E.G., Skull flexure from blast waves: a mechanism for brain injury with implications for helmet design, *PRL*, **103**:1087021-4, 2009.

[29] Mott, D.R., *et al.*, Blast-induced pressure fields beneath a military helmet, 20th International Symposium on Military Aspects of Blast and Shock, Oslo, Norway, 2008.

[30] Munson, B.R., Young, D.F., Okiishi, T.H., *Fundamentals of Fluid Mechanics*, 2nd Edition, J. Wiley & Sons, New York, 1994.

[31] Ofengeim, D. Kh., Drikakis, D., Simulation of blast wave propagation over a cylinder, *Shock Waves*, **7**:305-317, 1997.

[32] Okie, S., Traumatic brain injury in the war zone, *NEJM*, **352**:2043-2047, 2005.

[33] STAR-CCM+, v. 3.06, CD-Adapco, www.cd-adapco.com, 2008.

[34] Sun, M., *et al.*, Unsteady drag on a sphere by shock wave loading, *Shock Waves*, **14**(1-2):3-9, 2005

[35] Taber, K.H., Hayman, L.A., Diaz-Marchan, P.J., Rauch, R.A., Imaging of intracranial blood, in *Imaging of the nervous system*, Eds. Latchaw, R.E., Kucharczyk, J., Moseley, M.E., Elsevier Mosby, 555-575, 2005.

[36] Taber, K.H., Warden D.L., Hurley R.A., Blast-related traumatic brain injury: what is known?, *J Neuropsychiatry Clin Neurosci*, **18**(2):141-145, 2006.

[37] Tanno, H., *et al.*, Interaction of a shock with a sphere suspended in a vertical shock tube, *Shock Waves*, **13**:191-200, 2003.

[38] Taylor, P.A., Ford, C.C., Simulation of blast-induced early-time intracranial wave physics leading to traumatic brain injury, *J Biomech Eng*, **131**:0610071-11, 2009.

[39] *TM 5-855-1: Design and analysis of hardened structures to conventional weapons effects*, U.S. Army Techical Manual, August, 1998.

[40] Weiss, J.M., Smith, W.A., Preconditioning applied to variable and constant density flows, *AIAA J*, **33**(11):2050-2057, 1995.

[41] Weiss, J.M., Maruszewski, J.P., Smith, W.A., Implicit solution of preconditioned Navier-Stokes equations using algebraic multigrid, *AIAA J*, **37**(1):29-36, 1999.

[42] Wensheng, H., Onodera, O., Takayama, K., Unsteady interaction of shock wave diffracting around a circular cylinder in air, *Acta Mechanica Sinica*, **7**(4): 295-299, 1991.

[43] Yang, J.Y., Liu, Y., Lomax, H., Computation of shock wave reflection by circular cylinders, *AIAA J.*, **25**(5):683-689, 1987.

[44] Zaslavskii, *et al.*, Force action of a shock wave on a solid body, *J App Mech Tech Phys.*, **42**(3):533-537, 2001.

[45] Zeitzer, M.B., Brooks, J.M., In the line of fire: traumatic brain injury among Iraq war veterans, *AAOHN J*, **56**(8):347-353, 2008.

[46] Zoltak, J., Drikakis, D., Hybrid upwind methods for the simulation of unsteady shock-wave diffraction over a cylinder, *Comput. Methods Appl. Mech. Engrg.*, **162**:165-185, 1998.

Figure 1: Human model and computational domain (the head geometry is highlighted in light gray).

Figure 2: Transient pressure signatures at $r = 1.524$, 3.048, 4.572 m for the a) 0.6 kg and b) 3 kg equivalent TNT charges from the "one-dimensional" isolated blast simulations (5×10^{-4} to 0.008 m mesh resolutions). Inset: transient pressure signatures at $r = 4.572$ m for the "one-dimensional" (0.001 m mesh resolution) and three-dimensional (0.004 to 0.016 m mesh resolutions) isolated blast simulations.

Figure 3: a) Transient drag and b) lift force coefficients for a 0.08 m diameter sphere during the interaction with a planar shock wave of Mach number 1.22. The simulated values are for meshes with 45×10^3 to 648×10^3 cells. Inset: pressure distribution on the sphere at $t = 200.5 \times 10^{-6}$ s from the simulations and from Zaslavskii, *et al.'s* [44] model. Note that the values of $C_{x'}$ and $C_{y'}$ from Eqs. 3-4 are plotted only over the time during which the shock front intersects the sphere and $C_{y'}$ is computed over only one half ($y' \geq 0$) of the sphere.

Figure 4: Transient pressure signatures on the surface of the head at $y = 0$ for the a-f) 35×10^3 Pa and g-l) 88×10^3 Pa overpressure blast waves for different mesh resolutions (frontal facing orientation).

Figure 5: Density gradient contours across the surface of the model for the a-f) frontal and g-l) backward facing blast orientations (88×10^3 Pa overpressure blast wave). $t =$ a) 5.286×10^{-3} s, b) 5.351×10^{-3} s, c) 5.401×10^{-3} s, d) 5.562×10^{-3} s, e) 5.682×10^{-3} s, f) 5.872×10^{-3} s; $t =$ g) 5.400×10^{-3} s, h) 5.420×10^{-3} s, i) 5.460×10^{-3} s, j) 5.580×10^{-3} s, k) 5.820×10^{-3} s, l) 6.000×10^{-3} s.

Figure 6: a-e) Density gradient contours and f-j) pressure profiles at $y = 0$ for $t =$ a,f) 5.236×10^{-3} s, b,g) 5.396×10^{-3} s, c,h) 5.522×10^{-3} s, d,i) 5.687×10^{-3} s, e,j) 5.862×10^{-3} s (frontal facing orientation with the 88×10^3 Pa overpressure blast wave). The locus of the triple point, T_p, is denoted by the dashed line oriented at 60° to the horizontal in d). The vertical dashed lines in f-j) denote the start and end of the head along d_{nh}.

Figure 7: a-d) Density gradient contours and e-h) pressure profiles at $y = 0$ for $t =$ a,e) 5.460×10^{-3} s, b,f) 5.660×10^{-3} s, c,g) 5.820×10^{-3} s, d,h) 6.000×10^{-3} s (backward facing orientation with the 88×10^3 Pa overpressure blast wave). The locus of the triple point, T_p, is denoted by the dashed line oriented at 60° to the horizontal in d). The vertical dashed lines in e-h) denote the start and end of the head along d_{nh}.

Figure 8: Transient pressure signatures on the surface of the head at $y = 0$ for the 88×10^3 Pa overpressure blast wave (backward facing orientation).

Figure 9: Spatial-temporal plots of the pressure along the head and neck at $y = 0$ for the a,c) frontal and b,d) backward facing orientations corresponding to the a-b) 35×10^3 Pa and c-d) 88×10^3 Pa overpressure blast waves. The horizontal dashed lines denote the start and end of the head along d_{nh}. The contours highlight pressures that are equal to $p_0 + 0.25(p_{nr} - p_0)$ (solid white), $p_0 + 0.5(p_{nr} - p_0)$ (dashed white), and p_{nr} (solid black), where p_{nr} is the pressure due to the normal reflection of the incident blast wave (Eq. 2) at $r = 4.572$ m and p_0 is atmospheric pressure, 101×10^3 Pa. The white, dashed-dot contours denote pressures that are less than p_0.

Figure 10: Transient forces on the head for the a-b) frontal and c-d) backward facing cases with the a,c) 35×10^3 and b,d) 88×10^3 Pa overpressure blast waves. Note that the values of $F_{x'}$ and $F_{z'}$ from Eqs. 3-4 are plotted only over the time during which the shock front intersects the head.

Figure 11: Transient moment on the head about the occipital condyles ($\otimes$) for the a-b) frontal and c-d) backward facing cases with the a,c) 35×10^3 and b,d) 88×10^3 Pa overpressure blast waves. Note that the values of M_{oc} from Eq. 5-6 are plotted only over the time during which the shock front intersects the head.

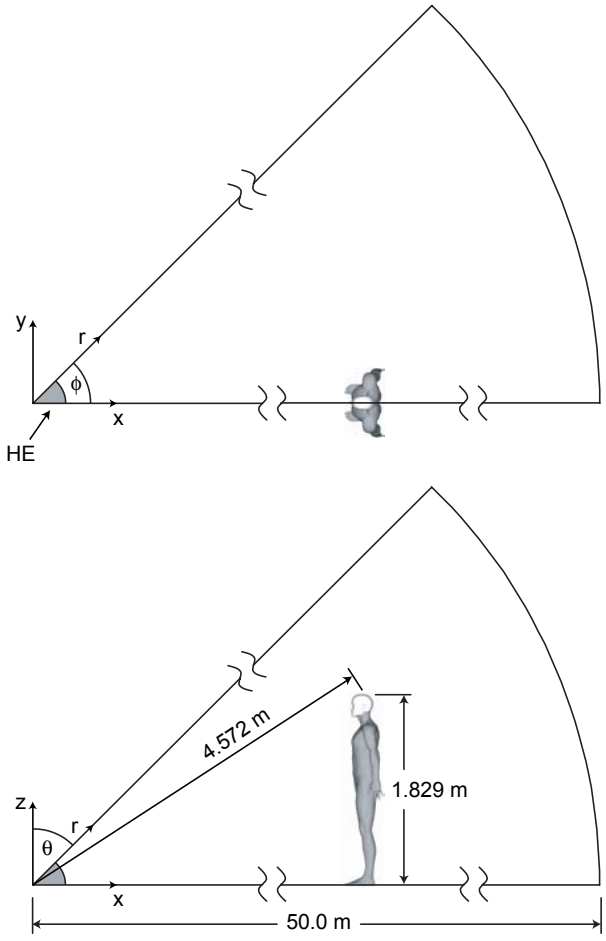

Figure 1. Ortega.

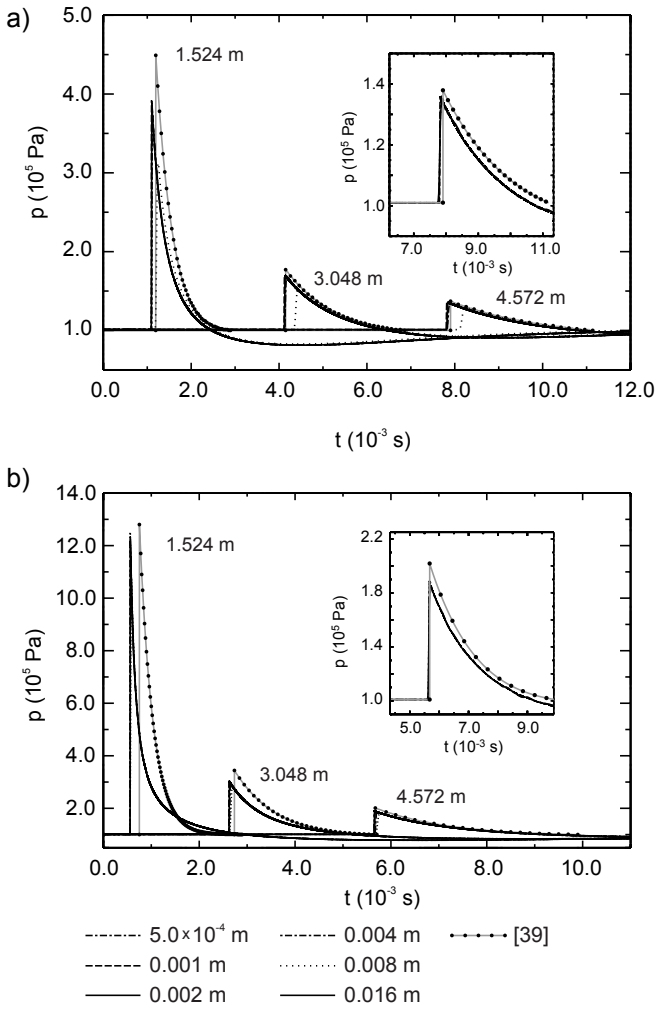

Figure 2. Ortega.

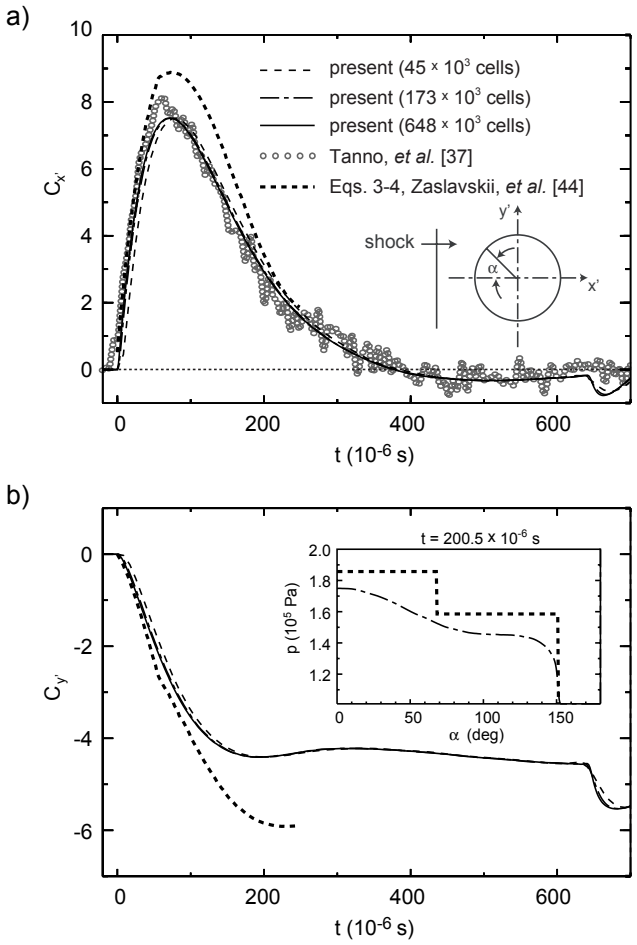

Figure 3. Ortega.

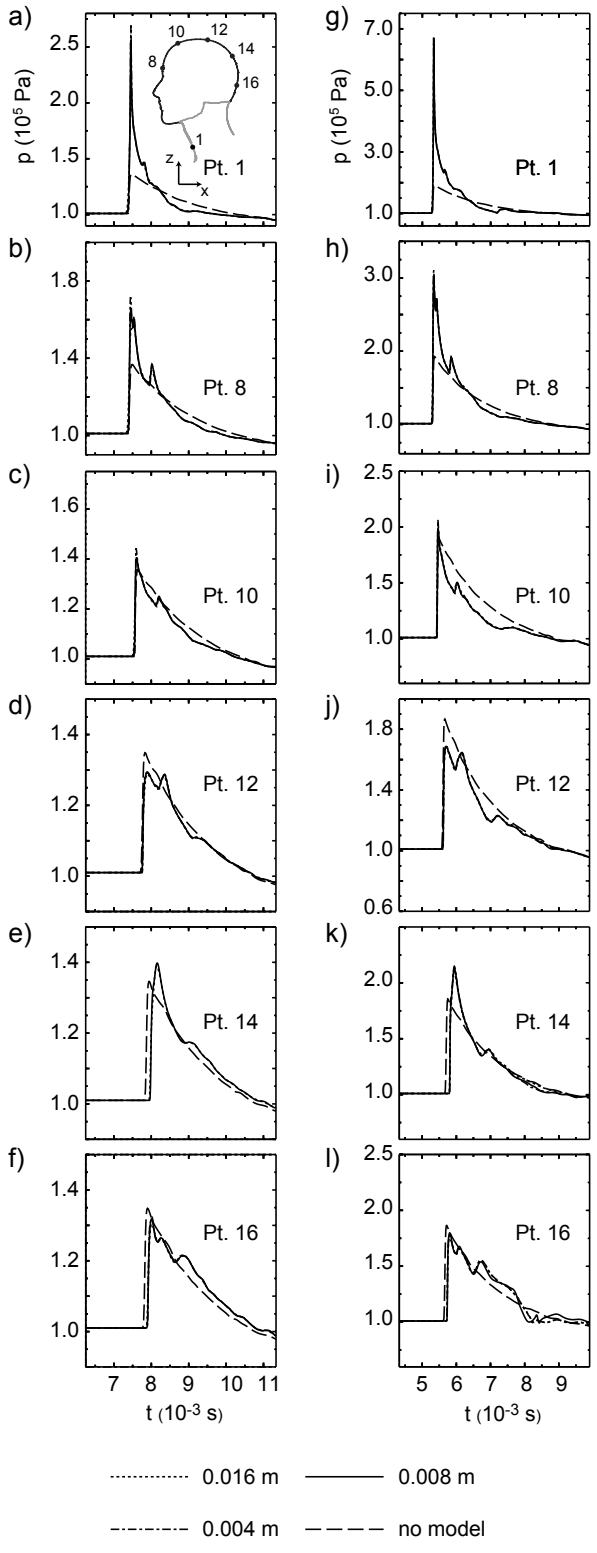

Figure 4. Ortega.

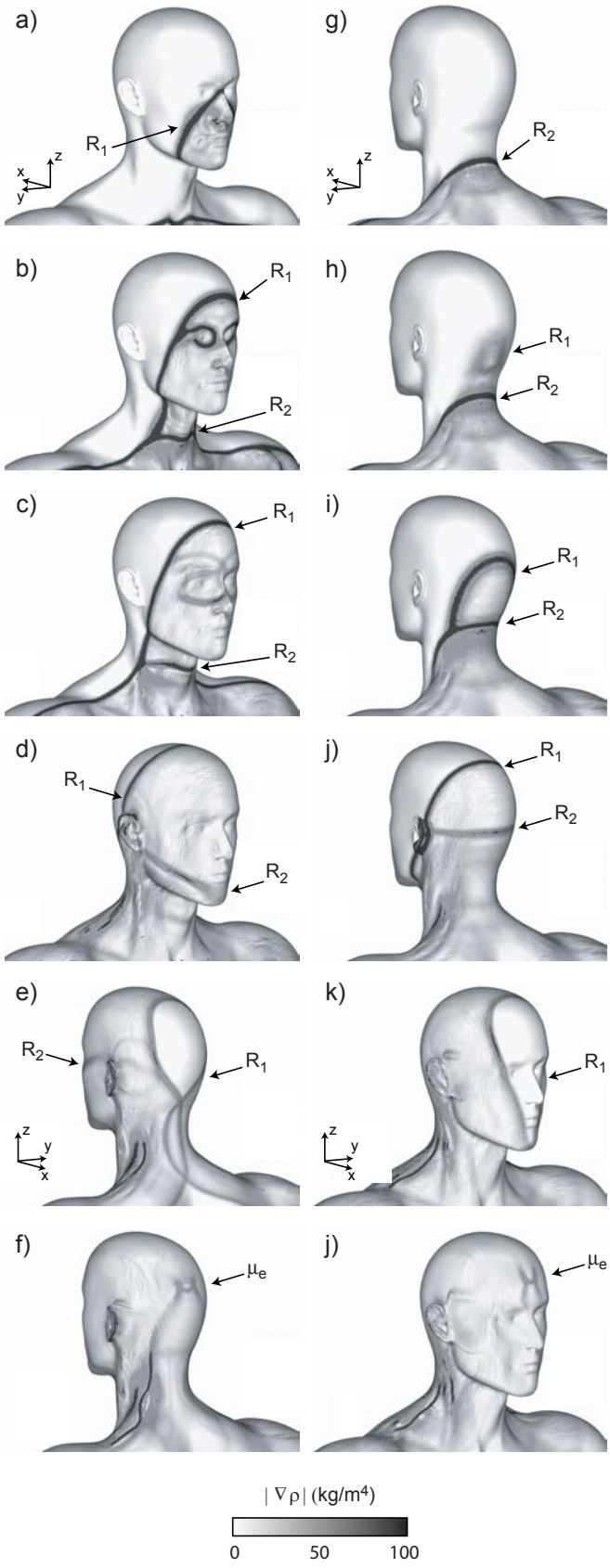

Figure 5. Ortega.

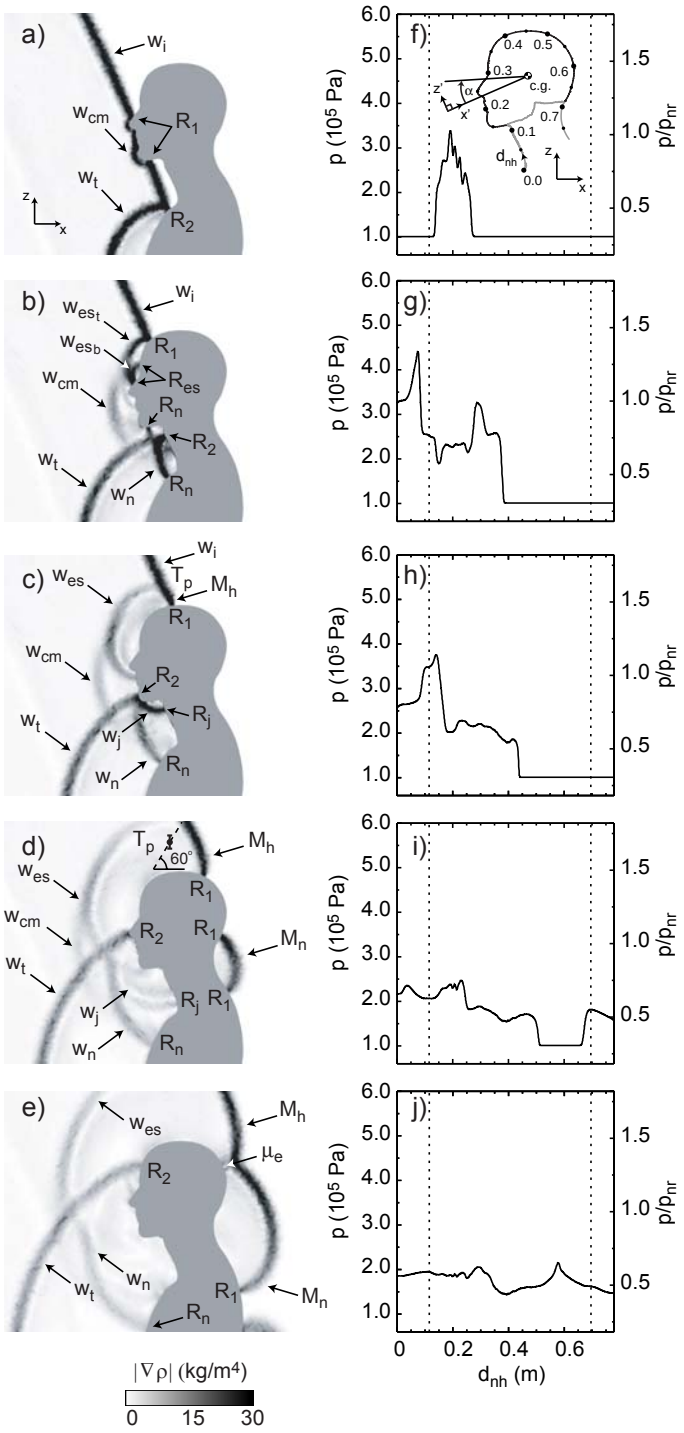

Figure 6. Ortega.

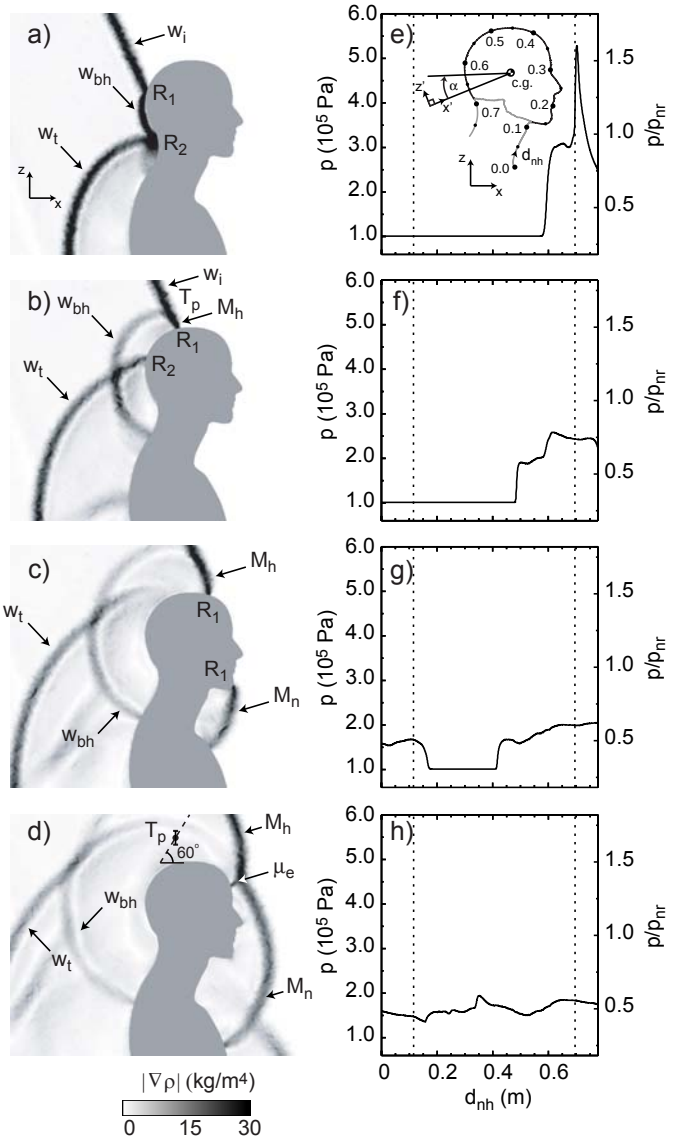

Figure 7. Ortega.

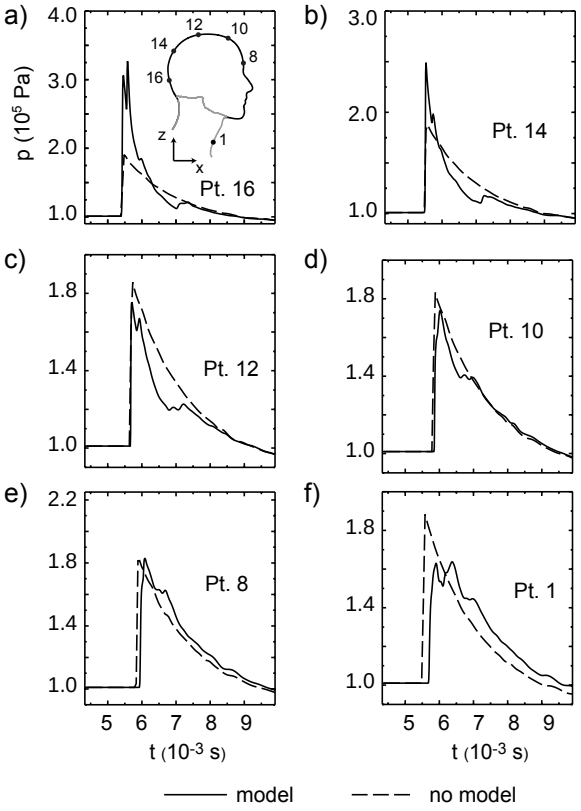

Figure 8. Ortega.

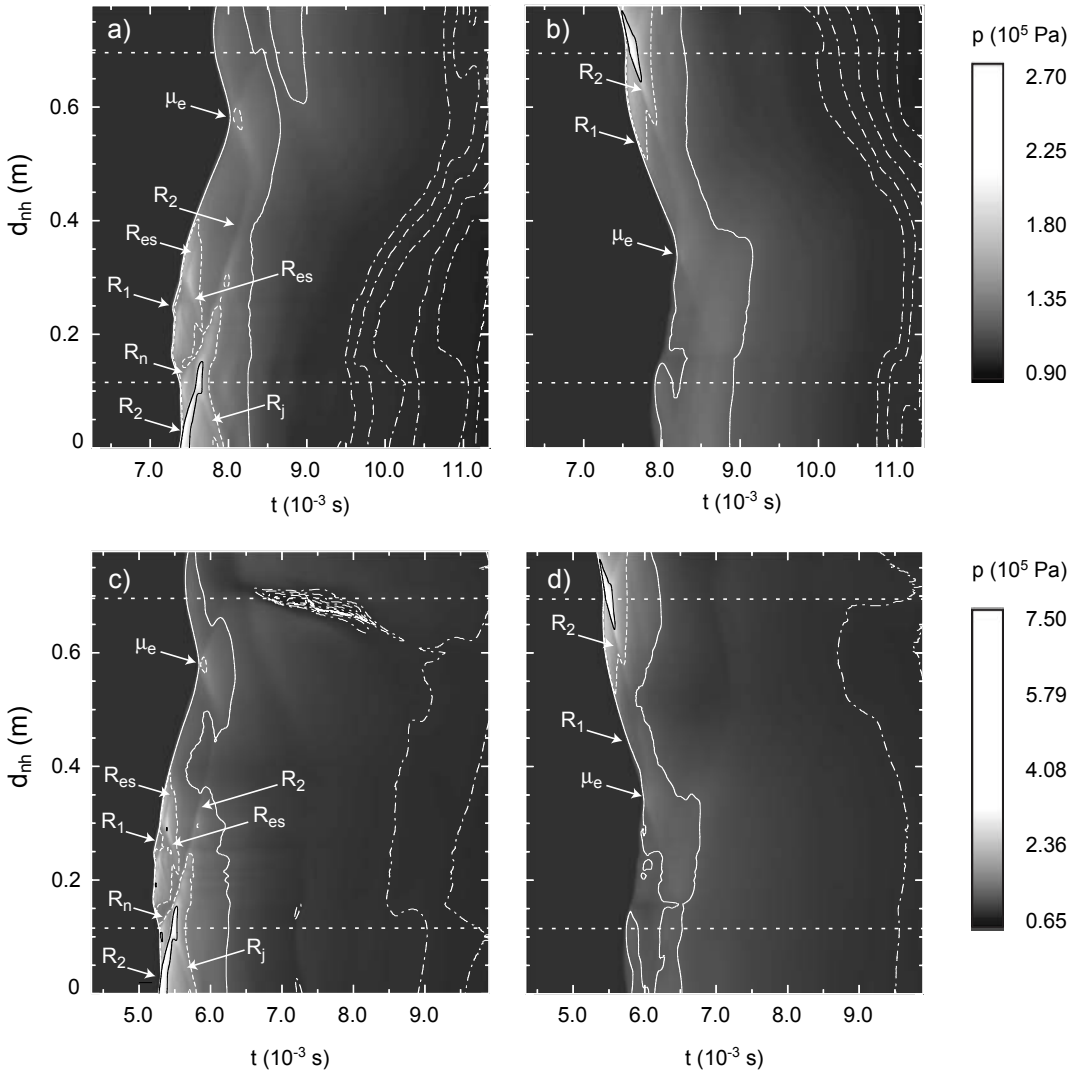

Figure 9. Ortega.

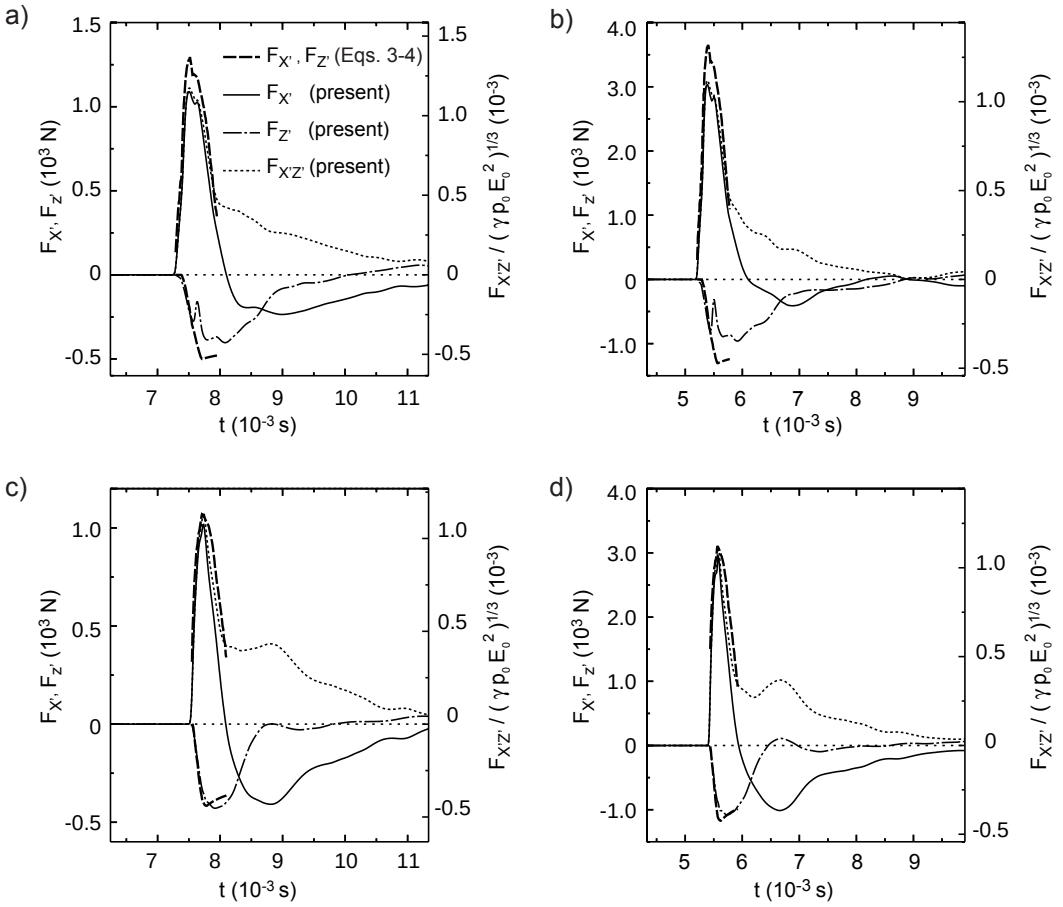

Figure 10. Ortega.

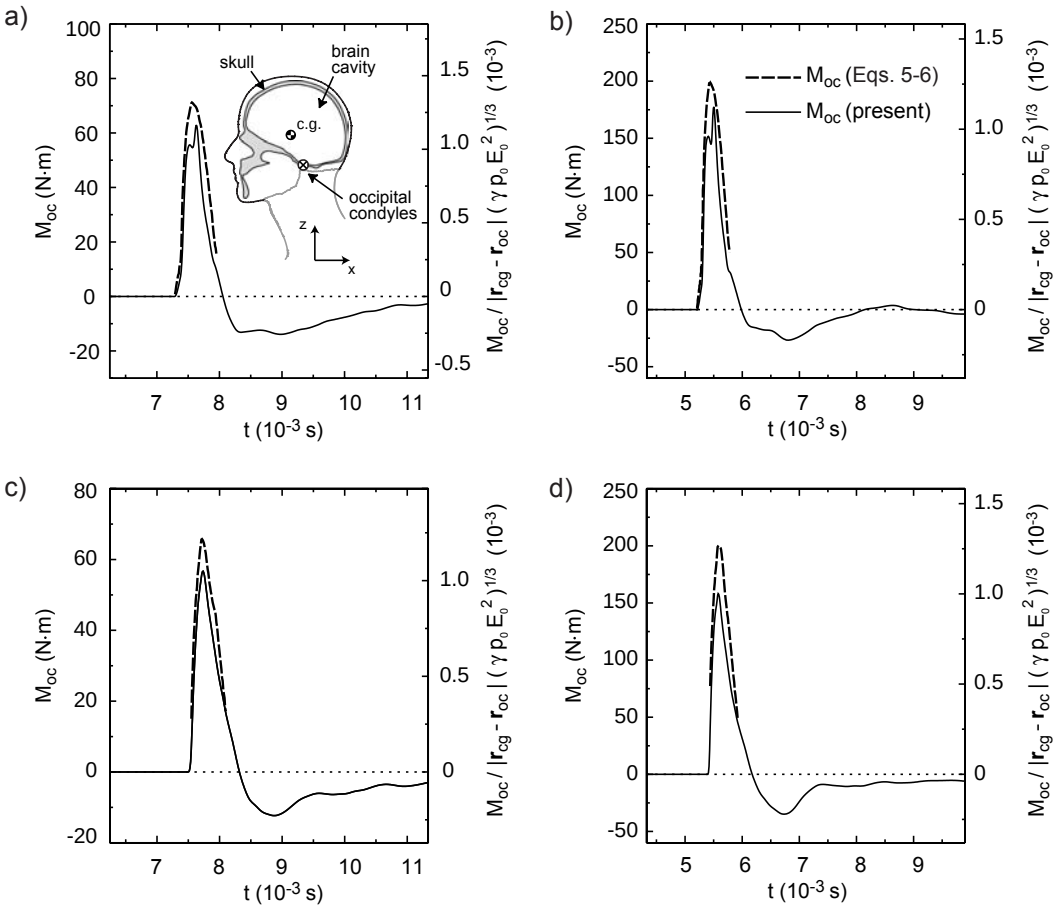

Figure 11. Ortega.